Enhanced spin pumping into superconductors provides evidence for superconducting pure spin currents

Kun-Rok Jeon,[1,2] Chiara Ciccarelli,[2*] Andrew J. Ferguson,[2] Hidekazu Kurebayashi,[3] Lesley F. Cohen,[4] Xavier Montiel,[5] Matthias Eschrig,[5] Jason W. A. Robinson,[1] and Mark G. Blamire[1*]

[1]Department of Materials Science and Metallurgy, University of Cambridge, 27 Charles Babbage Road, Cambridge CB3 0FS, UK

[2]Cavendish Laboratory, University of Cambridge, Cambridge CB3 0HE, UK

[3]London Centre for Nanotechnology and Department of Electronic and Electrical Engineering at University of College London, London WC1H 01H, UK

[4]The Blackett Laboratory, Imperial College London, SW7 2AZ, UK

[5]Department of Physics, Royal Holloway, University of London, Egham Hill, Egham, Surrey TW20 0EX, UK

*To whom correspondence should be addressed: cc538@cam.ac.uk, mb52@cam.ac.uk

Unlike conventional spin-singlet Cooper pairs, spin-triplet pairs can carry spin.[1,2] Triplet supercurrents were discovered in Josephson junctions with metallic ferromagnet (FM) spacers, where spin transport can only occur within the FM and in conjunction with a charge current. Ferromagnetic resonance (FMR) injects a pure spin current from a precessing FM into adjacent non-magnetic materials.[3,4] For spin-singlet pairing, FMR spin pumping efficiency decreases below the critical temperature (T_c) of a coupled superconductor (SC).[5,6] Here we present FMR experiments in which spin sink layers with strong spin-orbit coupling are added to the SC. Our results show that the induced spin currents, rather than being

suppressed, are substantially larger in the superconducting state compared with the normal state; although further work is required to establish the details of the spin transport process we show that this cannot be mediated by quasiparticles and is most likely a triplet pure spin supercurrent.

Direct spin transport studies in SCs[7-10] have traditionally involved quasiparticle (QP) injection at bias voltages around the superconducting gap energy. A number of exotic properties have been observed: enhanced spin relaxation time[11-13], spin and charge decoupling[9,10] and a giant spin-orbit interaction[14]. Equilibrium (zero-bias) studies[1,2] of the Josephson effect in SC/FM/SC junctions and T_c modulation in FM/SC/FM and SC/FM/FM' superconducting spin valves have demonstrated that engineered magnetically-inhomogeneous (spin-mixing) SC/FM interfaces can generate triplet pairing states. However, direct measurement of triplet spin transport through singlet SCs has not so far been achieved.

A time-dependent ferromagnetic magnetization generates a spin angular momentum flow into adjacent materials (spin pumping)[3,4], and the transport and relaxation of spin currents from the FM in turn affects its magnetization dynamics via an enhancement in the (effective) Gilbert damping α (Fig. 1a). Using this FMR method it was previously demonstrated[5] that Andreev reflection, in which the incident electron across the FM/SC interface is coherently coupled with the retro-reflection of a hole to generate a (spin-zero) spin-singlet Cooper pair in the SC, essentially excludes the transport of dynamically-driven spin currents through the superconducting gap 2Δ (Fig. 1b) and so the spin-current-induced broadening of the FMR linewidth is suppressed by the development of the superconducting state[6].

In this paper, we compare FMR results on Nb/$Ni_{80}Fe_{20}$/Nb trilayers with Pt/Nb/$Ni_{80}Fe_{20}$/Nb/Pt structures in which the Pt provides an effective spin sink with strong spin-orbit coupling (SOC). To explore the influence of superconductivity on spin transport we measured the temperature (T) evolution of the FMR spectra [e.g. the linewidth $\mu_0\Delta H$ (proportional to α) and the resonance field $\mu_0 H_{\mathrm{res}}$; see Supplementary Information (Sec. S1) for full details] across T_{c}. Where Pt (or other large SOC spin sinks) are present, a substantially increased FMR damping for SC layer thicknesses of the order of the coherence length ξ_{sc} is interpreted as evidence for the generation of superconducting spin currents.

Figure 2a shows $\mu_0\Delta H(T)$ for Nb/$Ni_{80}Fe_{20}$/Nb trilayers with several Nb thicknesses t_{Nb} at a fixed microwave frequency f = 20 GHz. For all t_{Nb}, $\mu_0\Delta H$ is almost T-independent between 10 and 100 K. All the samples show a slight upturn in $\mu_0\Delta H$ with decreasing T around 10 K. Since this also occurs for the non-superconducting sample (t_{Nb}=7.5 nm), this must reflect intrinsic normal state properties of the coupled system and be unrelated to peaks in $\mu_0\Delta H$ predicted below T_c associated with the onset of superconductivity[6,14]. As T is reduced further, a significant t_{Nb}-dependent reduction of $\mu_0\Delta H$ occurs which is explained by the inhibition of singlet spin transport in the SC[5,6,14]. To quantitatively characterize the overall behaviour, we plotted $\mu_0\Delta H(t_{Nb})$ for various T between 2 and 80 K (Fig. 2b). For all T, $\mu_0\Delta H(t_{\mathrm{Nb}})$ is approximately exponential, as expected for diffusive spin transport[3,4]. However, when T < 8 K (entering the superconducting state), $\mu_0\Delta H$ saturates faster to a smaller asymptotic value, implying that, below T_{c}, the transfer efficiency of spin across the $Ni_{80}Fe_{20}$/Nb interfaces and the characteristic length of spin transport in the Nb are both reduced[3,4]. This can be quantified, as discussed in Supplementary Information (Sec. S3).

The key aim of this work is to explore how this superconducting spin-blocking behaviour is modified when an effective spin sink is placed beyond the SC layers. Figure 2c shows $\mu_0\Delta H(T)$ for Pt/Nb/$Ni_{80}Fe_{20}$/Nb/Pt structures with different t_{Nb}. The most important aspect of the data is the remarkable enhancement of magnetization damping for the intermediate t_{Nb} of 15 and 30 nm at low T when attached to Pt layers. Note that for the thicker superconducting Nb layers (45 and 60 nm), the T dependence of $\mu_0\Delta H$ is qualitatively similar to the samples without the Pt layers (Fig. 2a). For comparison with Fig. 2b, we show in Fig. 2d $\mu_0\Delta H(t_{Nb})$ for different (constant) T ranging from 80 to 2 K. There is a clear enhancement of $\mu_0\Delta H$ in the superconducting state for the t_{Nb} = 15 and 30 nm samples. The change in $\mu_0\Delta H$ between the normal and superconducting states is shown in the upper inset of Fig. 2d which contains data for other t_{Nb} and shows a systematic enhancement up to t_{Nb} = 30 nm followed by a fall for larger thicknesses.

Before discussing the likely explanation for this enhancement of spin transport in the superconducting state, we first consider the normal state using the spin pumping model[3,4] for composite spin sinks:

$$\alpha_{sp}^{c}(t_{SC}) = 2\cdot\left(\frac{g_L\mu_B g_r^{\uparrow\downarrow}}{4\pi M_s t_{FM}}\right)\cdot\left[1+g_r^{\uparrow\downarrow}\mathcal{R}_{SC}\cdot\left(\frac{1+\ g\mathcal{R}_{SC}\cdot\tanh\left(\frac{t_{SC}}{l_{sd}^{SC}}\right)}{\tanh\left(\frac{t_{SC}}{l_{sd}^{SC}}\right)+\ g\mathcal{R}_{SC}}\right)\right]^{-1}, \qquad (1)$$

where g_L is the Landé g-factor, μ_B is the Bohr magneton, and $\hbar$ is Plank's constant divided by 2π. $g_r^{\uparrow\downarrow}$ is the (effective) spin mixing conductance of the $Ni_{80}Fe_{20}$/Nb interface and g is the (effective) spin transfer conductance of the Nb/Pt interface (~35 nm^{-2})[3,15]. $\mathcal{R}_{SC} \equiv \rho_{SC} l_{sd}^{SC} e^2/2\pi\hbar$ is the spin resistance of the Nb layer where ρ_{SC} is the resistivity of the Nb [see Supplementary Information (Sec. S3)], l_{sd}^{SC} is the spin diffusion length of the Nb, and e is the electron charge. t_{FM} is the $Ni_{80}Fe_{20}$ thickness and M_s is its saturation magnetization. For $T \geq 8$ K, the universal trend of decreasing $\mu_0\Delta H$ with increasing t_{Nb} is well fitted by this model (Fig. 2d, solid lines). This is a result of the progressively increased screening of the Pt spin sink from the $Ni_{80}Fe_{20}$ spin source as the Nb layer thickness increases, the Nb having a modest spin conductance [3.5 – 5.0 nm^{-2}, see Supplementary Information (Sec. S3)]. The extracted values of $g_r^{\uparrow\downarrow}$ (~10 nm^{-2}) and l_{sd}^{SC} (35 – 45 nm) are also in good agreement with those obtained from the samples without Pt layers [g = 0, see Figs. 2b and S3 (Supplementary Information)] and, for l_{sd}^{SC}, with Ref.[16]. It can be seen that the FMR linewidth tends to the same value at large t_{Nb} for samples with and without the Pt spin sinks as would be expected once spin transport to the Pt is blocked.

For the superconducting state, we consider first the samples without the Pt spin sinks. The transmission of non-equilibrium spin accumulation generated on the FM side to the nonmagnetic layer depends on the matching of the electronic band structures in the two materials on either side of the interface[17,18], which can be quantified as follows:

$$\mathcal{T} = \frac{g_0^{\uparrow\downarrow}}{g_0^{\uparrow\downarrow} + \left(\frac{1}{\mathcal{R}_{FM}} \cdot \tanh\left(\frac{t_{FM}}{l_{sd}^{FM}}\right)\right)} \quad ; \qquad g_0^{\uparrow\downarrow} = \frac{g_r^{\uparrow\downarrow} \cdot \left(\frac{1}{\mathcal{R}_{FM}} \cdot \tanh\left(\frac{t_{FM}}{l_{sd}^{FM}}\right)\right)}{\left(\frac{1}{\mathcal{R}_{FM}} \cdot \tanh\left(\frac{t_{FM}}{l_{sd}^{FM}}\right)\right) - g_r^{\uparrow\downarrow}} \qquad (2)$$

where $\mathcal{R}_{FM} \equiv \rho_{FM} l_{sd}^{FM} e^2/2\pi\hbar$, ρ_{FM} is the resistivity (20 $\mu\Omega$-cm for $T \leq 10$ K, 30 $\mu\Omega$-cm at 300 K) of the $Ni_{80}Fe_{20}$[19], and l_{sd}^{FM} is the spin diffusion length (5 nm for $T \leq 10$ K, 4 nm at 300 K). Note that $g_0^{\uparrow\downarrow}$ is the actual spin mixing conductance. $\mathcal{T}$ is calculated to be 0.34, 0.34, 0.51, and 0.59 at 2, 4, 8, and 300 K, respectively, using Eq. (2). We can then see that the spin transparency of the $Ni_{80}Fe_{20}$/Nb interface is much lower when the Nb is superconducting, supporting that the reduced spin-injection efficiency which is ascribed to the band structure mismatch due to the presence of the energy gap 2Δ. For the transport length l_{qp}^{sp} of dynamically-driven spin-polarized QPs in the diffusive [$t_{\mathrm{Nb}} > l_{mfp}$, where l_{mfp} is the mean free path of the Nb (6 nm)] and low T condition ($T/T_c \leq 0.3$)[16], one has to take into account the conversion time τ_{AR} of QPs into (spin-singlet) Cooper pairs by Andreev reflection in addition to their spin lifetime τ_{sf}:

$$l_{qp}^{sp} = \sqrt{D \cdot \left(\frac{1}{\tau_{AR}} + \frac{1}{\tau_{sf}}\right)^{-1}} \qquad (3)$$

where D is the diffusion coefficient of the Nb. Considering that τ_{AR} (for low energy QPs) is much shorter than τ_{sf} as Andreev reflection is fundamentally the interfacial conversion process, Eq. (3) can be simplified to $l_{qp}^{sp} \approx \sqrt{D\tau_{AR}}$, which therefore can be comparable to ξ_{sc}.[16] In fact, we find that the estimated l_{qp}^{sp} of ~21 nm at 2 K is of the order of the zero-temperature ξ_{sc} of Nb (13 nm) in the dirty limit, given by $0.85\sqrt{l_{mfp} \cdot \xi_0}$ where ξ_0 is the clean-limit coherence length of Nb (38 nm). We note that in a previous experiment of the magnetoresistance of an $Ni_{80}Fe_{20}$/Nb/$Ni_{80}Fe_{20}$ spin valve[16], the penetration length of spin-polarized QPs through superconducting Nb was measured to be ~16 nm under low T and DC bias conditions.

This general behaviour is replicated by the t_{Nb} = 45 and 60 nm Pt/Nb/$Ni_{80}Fe_{20}$/Nb/Pt samples (Fig. 2c) in that the transport of spin-polarized QPs is blocked by Andreev reflection. The anomalous Pt/Nb/$Ni_{80}Fe_{20}$/Nb/Pt samples (t_{Nb} = 15, 22.5, 30 and 37.5 nm, Fig. 2d) behave in an exactly opposite way in that the FMR linewidth and hence spin transport to the Pt is progressively *enhanced relative to the normal state* with decreasing T.

The enhanced spin cannot carried by QP currents even if one assumes an unexpected increase in the low T spin diffusion length because the available QP states will progressively freeze out at a lower T, as demonstrated by our own measurements of

$Nb/Ni_{80}Fe_{20}/Nb$ samples as well as the existing theories of QP-mediated spin transport[5,6]. It should be noted that the significant enhancement of FMR linewidth predicted for *insulating* FM/SC[6] occurs only close to T_c and is strongly suppressed for conducting FM materials. The existing theory for FMR in metallic FM/SC systems also shows a significant damping of QP spin transport even if a spin sink layer is added to the SC[5]. Thus the monotonic enhancement of spin transport with decreasing T for the intermediate t_{Nb} must involve supercurrents. The mechanisms enabling supercurrent-mediated spin transport through a singlet SC are crossed Andreev reflection (CAR), elastic co-tunneling (EC), or an induced triplet pairing state[20]. CAR and EC via spin-singlet supercurrents require the involvement of (unpaired) electrons within 2Δ in both the FM and the spin sink. In order to distinguish between these mechanisms, we have replaced the Pt with a range of other spin sink materials for fixed t_{Nb} = 30 nm (Fig. 3a). Of the materials used: 5 nm-thick Ta proximity-coupled to Nb should have an induced gap almost equal to that of the Nb[21] and much larger than the spin-splitting of the electrochemical potentials $\Delta\mu$ (a few μeV) induced by spin pumping at the $Ni_{80}Fe_{20}/Nb$ interface [see Supplementary Information (Sec. S7) for details] which eliminates the CAR and EC processes; in contrast, $Fe_{50}Mn_{50}$ strongly suppresses the Nb gap[22] and so makes these processes more possible. The experimental results (Fig. 3b), which show superconducting spin transport relative to the normal state strongly enhanced by Ta and suppressed by $Fe_{50}Mn_{50}$, are therefore incompatible with these processes. The remaining possibility is therefore that the spin is carried via spin-triplet supercurrents.

A variety of mechanisms for generating triplet states have been proposed: static magnetic-inhomogeneity at the SC/FM interface[23-25], SOC in conjunction with an exchange field[26,27], and the precession of interface magnetization[28,29]; in all cases long-ranged triplet pairs (generated at the SC interface) should also penetrate into the SC side and decay over the length scale of ξ_{SC}. Since our structures contain a single homogeneous FM layer which is precessing coherently, the first mechanism appears to be irrelevant.

It is interesting to note that in addition to strong SOC, Pt is close to a ferromagnetic instability which induces a high spin susceptibility[30]; therefore in this case, a corrective term including the electron-electron interactions would need to be taken into account in any rigorous theoretical model[26-29]. Such a term, which is always present in real metallic materials, but is enhanced in Pt, leads to a non-negligible spin-splitting in the Pt layer resulting from the short-range triplet correlations and the spin penetration[2]. Our preliminary calculations suggest that in this scenario, long-range spin-triplet correlations would then be produced across the Nb layer between the precessing $Ni_{80}Fe_{20}$ and the spin-split Pt giving rise to an additional spin-polarized supercurrent below T_c. This additional spin supercurrent would be expected to increase below T_c and decreases with a thicker Nb layer, consistent with our experimental observations. Our experiments on other materials (Fig. 3b) show that the elements with large SOC (Pt, W, Ta)[31] reveal a large enhancement compared with the other materials, implying that SOC, possibly acting in conjunction with a spin-splitting due to Fermi liquid effects may provide the underlying explanation.

We have shown that FMR spin pumping into singlet SCs terminated by a large (SOC) spin sink more efficiently transfers angular momentum than in the normal state. Although detailed theories need to be developed to explain these results, we have demonstrated that the spin currents cannot be carried by quasiparticles and are most likely carried by spin-triplet pairs. We believe that the results presented in this paper provide evidence for spin-polarized supercurrents in SCs.

Methods

Methods and any associated references are available in the online version of the paper.

References

1. Linder, J. & Robinson, J. W. A. Superconducting Spintronics. *Nature Phys.* **11**, 307–315 (2015).
2. Eschrig, M. Spin-polarized supercurrents for spintronics: a review of current progress. *Rep. Prog. Phys.* **78**, 104501 (2015).
3. Tserkovnyak, Y., Brataas, A., Bauer, G. E. W. & Halperin, B. I. Nonlocal magnetization dynamics in ferromagnetic heterostructures. *Rev. Mod. Phys.* **77**, 1375-1421 (2005).
4. Ando, K. *et al.* Inverse spin-Hall effect induced by spin pumping in metallic system. *J. Appl. Phys.* **109**, 103913 (2011).
5. Bell, C., Milikisyants, S., Huber, M. & Aarts, J. Spin Dynamics in a Superconductor-Ferromagnet Proximity System. *Phys. Rev. Lett.* **100**, 047002 (2008).
6. Morten, J. P., Brataas, A., Bauer, G. E. W., Belzig, W. & Tserkovnyak, Y. Proximity-effect-assisted decay of spin currents in superconductors. *Europhysics Lett.* **84**, 57008 (2008).
7. Beckmann, D. Spin manipulation in nanoscale superconductors. *J Phys: Condens. Matter* **28**, 163001 (2016).
8. Hübler, F., Wolf, M. J., Beckmann, D. & v. Löhneysen, H. Long-Range Spin-Polarized Quasiparticle Transport in Mesoscopic Al Superconductors with a Zeeman Splitting. *Phys. Rev. Lett.* **109**, 207001 (2012).
9. Quay, C. H. L., Chevallier, D., Bena, C. & Aprili, M. Spin imbalance and spin-

charge separation in a mesoscopic superconductor. *Nature Phys.* **9**, 84-88 (2013).

10. Wakamura, T., Hasegawa, N., Ohnishi, K., Niimi, Y. & Otani, Y. Spin Injection into a Superconductor with Strong Spin-Orbit Coupling. *Phys. Rev. Lett.* **112**, 036602 (2014).
11. Yang, H., Yang, S.-H., Takahashi, S., Maekawa, S. & Parkin, S. S. P. Extremely long quasiparticle spin lifetimes in superconducting aluminium using MgO tunnel spin injectors. *Nature Mater.* **9**, 586-593 (2010).
12. Poli, N. *et al.* Spin injection and relaxation in a mesoscopic superconductor. *Phys. Rev. Lett.* **100**, 136601 (2008).
13. Wakamura, T. *et al.* Quasiparticle-mediated spin Hall effect in a superconductor. *Nature Mater.* **14**, 675–678 (2015).
14. Inoue, M., Ichioka, M. & Adachi, H. Spin pumping into superconductors: A new probe of spin dynamics in a superconducting thin film. *Phys. Rev. B* **96**, 024414 (2017).
15. Rojas-Sanchez, J. C. *et al.* Spin pumping and inverse spin Hall effect in platinum: the essential role of spin-memory loss at metallic interfaces. *Phys. Rev. Lett.* **112**, 106602 (2014).
16. Gu, J. Y., Caballero, J. A., Slater, R. D., Loloee, R. & Pratt, W. P. Direct measurement of quasiparticle evanescent waves in a dirty superconductor. *Phys. Rev. B* **66**, 140507 (2002).
17. Brataas, A., Nazarov, Y. V. & Bauer, G. E. W. Finite-element theory of transport in ferromagnet-normal metal systems. *Phys. Rev. Lett.* **84**, 2481-2484 (2000).
18. Zhang, W., Han, W., Jiang, X., Yang, S.-H. & S. P. Parkin, S. Role of transparency of platinum–ferromagnet interfaces in determining the intrinsic magnitude of the spin Hall effect. *Nature Phys.* **11**, 496-502 (2015).

19. Villamor, E., Isasa, M., Hueso, L. E. & Casanova, F. Temperature dependence of spin polarization in ferromagnetic metals using lateral spin valves. *Phys. Rev. B* **88**, 184411 (2013).

20. Flokstra, M. G. *et al.* Remotely induced magnetism in a normal metal using a superconducting spin-valve. *Nature Phys.* **12**, 57-61 (2016).

21. Ruggiero, S. T., Track, E. K., Prober, D. E., Arnold, G. B. & DeWeert, M. J. Electron tunneling in tantalum surface layers on niobium. *Phys. Rev. B* **34**, 217-225 (1986).

22. Bell, C. *et al.* Proximity and Josephson effects in superconductor/antiferromagnetic Nb/gamma-Fe50Mn50 heterostructures. *Phys. Rev. B* **69**, 109903 (2003).

23. Grein, R., Löfwander, T. & Eschrig, M. Inverse proximity effect and influence of disorder on triplet supercurrents in strongly spin-polarized ferromagnets. *Phys. Rev. B* **88**, 054502 (2013).

24. Kalcheim, Y., Millo, O., Di Bernardo, A., Pal, A. & Robinson, J. W. A. Inverse proximity effect at superconductor-ferromagnet interfaces: Evidence for induced triplet pairing in the superconductor. *Phys. Rev. B* **92**, 060501(R) (2015).

25. Di Bernardo, A. *et al.* Signature of magnetic-dependent gapless odd frequency states at superconductor/ferromagnet interfaces. *Nature Commun.* **6**, 8053 (2015).

26. Bergeret, F. S. & Tokatly, I. V. Spin-orbit coupling as a source of long-range triplet proximity effect in superconductor-ferromagnet hybrid structures. *Phys. Rev. B* **89**, 134517 (2014).

27. Jacobsen, S. H., Kulagina, I. & Linder, J. Controlling superconducting spin flow with spin-flip immunity using a single homogeneous ferromagnet. *Sci. Rep.* **6**, 23926 (2016).

28. Houzet, M. Ferromagnetic Josephson Junction with Precessing Magnetization.

Phys. Rev. Lett. **101**, 057009 (2008).

29. Holmqvist, C., Teber, S. & Fogelström, M. Nonequilibrium effects in a Josephson junction coupled to a precessing spin. *Phys. Rev. B* **83**, 104521 (2011).
30. König, R., Schindler, A. & Herrmannsdörfer, T. Superconductivity of Compacted Platinum Powder at Very Low Temperatures. *Phys. Rev. Lett.* **82**, 4528-4531 (1999).
31. Tanaka, T. *et al.* Intrinsic spin Hall effect and orbital Hall effect in 4d and 5d transition metals. *Phys. Rev. B* **77**, 165117 (2008).

Acknowledgements

This work was supported by EPSRC Programme Grant EP/N017242/1.

Author contributions

K.-R.J. and M.G.B. conceived and designed the experiments; The samples were prepared by K.-R.J, with help and sputtering system provided by J.W.A.R. and M.G.B; The FMR measurements were carried out by K.-R.J. with help of C.C., H.K. and A.J.F.; The model calculation was done by X.M. and M.E. whereas the data analysis was done by K.-R.J., C.C., H.K., J.W.A.R. and M.G.B.; All authors discussed the results and commented on the manuscript, which was written by K.-R.J. and M.G.B.

Additional information

The authors declare no competing financial interests. Supplementary information accompanies this paper on www.nature.com/naturematerials. Reprints and permissions information is available online at http://npg.nature.com/reprintsandpermissions. Correspondence and requests for materials should be addressed to C.C. or M.G.B.

Competing interests

The authors declare no competing financial interests.

Methods

Sample preparation. The heterostructures were grown on 5 mm × 5 mm quartz substrates by dc magnetron sputtering in an ultra-high vacuum chamber. The chamber was baked out for 10 hours and subsequently cooled with a liquid nitrogen for 2 hour to reach a base pressure better than 5×10^{-6} Pa and a water partial pressure below 10^{-7} Pa. All layers were grown *in-situ* at room temperature. Nb, $Ni_{80}Fe_{20}$, and Cu (capping layer present on all samples) were deposited at an Ar pressure of 1.5 Pa and Pt at 3.0 Pa. The typical deposition rates were 21.1 nm/min for Nb, 5.1 nm/min for $Ni_{80}Fe_{20}$, 7.6 nm/min for Pt, and 9.7 nm/min for Cu. Multiple quartz substrates were placed on a rotating circular table which passed in series under stationary magnetrons, so that 5 samples with different layer thicknesses could be grown in the same deposition run. This guarantees that the interface properties of the samples presented are more or less identical. The thickness of each layer was controlled by adjusting the angular speed of the rotating table at which the substrates moved under the respective targets and the sputtering power. The thicknesses of Py, Pt, and Cu layers were kept constant at 6, 5, and 5 nm, respectively, while the thickness of Nb layer varied from 7.5 to 60 nm in order to investigate the variation of FMR linewidth as a function of Nb thickness through the superconducting transition T_c. For the study of spin-sink material dependence (Fig. 3), Ta and W were grown at an Ar pressure of 3.0 Pa whereas Cu (spin sink layer), Ho, and $Fe_{50}Mn_{50}$ were of 1.5 Pa to keep the interface roughness more or less similar for all samples.

Superconducting transition measurement. DC electrical transport measurements were mostly conducted using a custom-built dipstick probe in a liquid helium dewar with a four-point current-voltage method. The resistance R (of a sample) vs. temperature T curves were obtained while decreasing T. From the T derivative of R, dR/dT, the superconducting transition temperature T_c was denoted as the T value that exhibits the maximum of dR/dT. Note that care was taken to ensure that the applied current $I \leq 0.1$ mA had no effect on T_c. For the samples with T_c below 4.25 K, the electrical transport measurements were performed in a closed-cycle cryostat with a ^{3}He insert capable of reaching 0.3 K. The full set of $R(T)$ curves is included in the Supplementary Information (Sec. S9).

Dynamic measurement technique. The broad-band FMR setup used for this study involves a microwave (MW) source, lock-in amplifier (LIA), and co-planar waveguide (CPW). The MW source whose power is of −20 to +20 dBm is connected to a pulse generator so that a MW frequency f_{mw} (in the GHz range) is squarely modulated with a modulation frequency f_{mod} of <1 kHz. The transmitted MW signal through a sample attached onto a CPW is rectified by a MW diode with a bandwidth of 40 GHz. The LIA multiplies the diode voltage with a reference at f_{mod} and integrates the result over a certain time. This results in a DC voltage, only coming from signals having the same frequency as the reference. To obtain each FMR spectrum, this DC voltage was measured while sweeping the external magnetic field (along the film plane direction) at a fixed f_{mw} of 5 to 20 GHz. The MW power was set to 10 dBm for all measurements but taking into account the attenuation through coaxial cables and connectors, the actual MW power absorbed in the sample is expected to be a few mW [see the Supplementary Information (Sec. S11) for discussion about the effect of MW power on the superconductivity of Nb]. Note that in any case, the thickness of Nb layers studied here is much less than the magnetic penetration depth (> 100 nm in thin Nb films)[32] and so there is no significant effect of Meissner screening on the local (DC/RF) magnetic field experienced by $Ni_{80}Fe_{20}$ below T_c. We employed a vector field cryostat from *Cryogenic Ltd* that allows for a 1.2 T magnetic field in any direction over a wide T range of 2 − 300 K. Most of the room temperature measurements were performed by using a separate FMR setup capable of a (DC) magnetic field modulation, which provides a better signal-to-noise ratio. Note also that we ensured that there is no fundamental difference in the obtained FMR spectra (at 300 K) between the two setups.

References

32. Gubin, A. I., Il'in, K. S., Vitusevich, S. A., Siegel, M. & Klein, N. Dependence of magnetic penetration depth on the thickness of superconducting Nb thin films. *Phys. Rev. B* **72**, 064503 (2005).

Data availability.

The data used in this paper can be accessed at https://doi.org/10.17863/CAM.20719

Figure legends

Figure 1. Principle of the approach. a-b, Schematic of magnetization dynamics and resulting spin transport in a symmetric FM/SC/FM (FM: ferromagnet, SC: superconductor) structure above (**a**) and below (**b**) the superconducting transition

temperature T_c. Spin-dependent density of states and its occupation in SCs are indicated by the orange (majority-spin) and cyan (minority-spin) symbols. M(t), J_s, and α_0 (α_{sp}) represent, respectively, the time-varying magnetization vector of the FM, the net spin current injected from the FM into the SC by spin pumping, and the Gilbert damping of the FM irrelevant (relevant) to the spin pumping. $\mu^{\uparrow}$ and $\mu^{\downarrow}$ are the spin-dependent electrochemical potentials. Note that the dark blue indicates the region in which the superconducting energy gap Δ is suppressed close to the FM/SC interface due to the (inverse) proximity effect, resulting in the spatial variation of 2Δ over the superconducting coherence length ξ_{sc} (from the FM/SC interface).

Figure 2. Enhanced spin transport in the superconducting state when coupled to strong spin sink. a, Temperature T dependence of the FMR linewidth $\mu_0\Delta H$ (top) and the resonance magnetic field $\mu_0 H_{res}$ (bottom) for various Nb thicknesses. The dashed lines indicate their T_c. **b,** FMR linewidth $\mu_0\Delta H$ as a function of Nb thickness t_{Nb} of Nb/$Ni_{80}Fe_{20}$/Nb samples at various T. The solid lines are fits to estimate the effective values of spin mixing conductance and spin diffusion length using the spin pumping model[3,4]. The inset shows data and fits for 300 K. In this inset, the t_{Nb} dependence of the Gilbert damping constant α (red symbol) is also shown for comparison. **c,** data equivalent to (**a**) but for Pt/Nb/$Ni_{80}Fe_{20}$/Nb/Pt spin sink samples. **d,** data equivalent to (**b**) but for Pt/Nb/$Ni_{80}Fe_{20}$/Nb/Pt spin sink samples; the same colour coding applies for the different T. The upper-right inset of (**d**) exhibits the t_{Nb} dependence of the FMR linewidth difference across T_c, defined as $\mu_0\Delta H(2\text{ K}) - \mu_0\Delta H(8\text{ K})$. The red dashed line in this inset is a guide to the eyes; the rectangular and diamond symbols represent two independent sets of the samples grown each in a single deposition run [see Supplementary Information (Sec. S12) for details]. Error bars denote standard deviation

of multiple measurements.

Figure 3. Enhanced spin transport in the superconducting state enabled by spin-orbit coupling (SOC) along with precessing magnetization. a, FMR linewidth $\mu_0\Delta H$ as a function of the normalized temperature T/T_c for various spin sink materials with a constant thickness of 5 nm, taken at the fixed t_{Nb} = 30 nm and f = 20 GHz. The Ref sample is t_{Nb} = 30 from the series shown in Fig. 2a which only has a 5-nm Cu (top) cap layer. **b**, Spin-sink material dependence of the FMR linewidth difference across T_c, denoted as $\mu_0\Delta H$(2 K) − $\mu_0\Delta H$(8 K). Note that the resonance field $\mu_0 H_{res} \geq 350$ mT induces a homogeneous magnetization M in Ho (5 nm), enabling to focus on SOC[26,27] rather than M inhomogeneity[1,2]. Error bars denote standard deviation of multiple measurements.

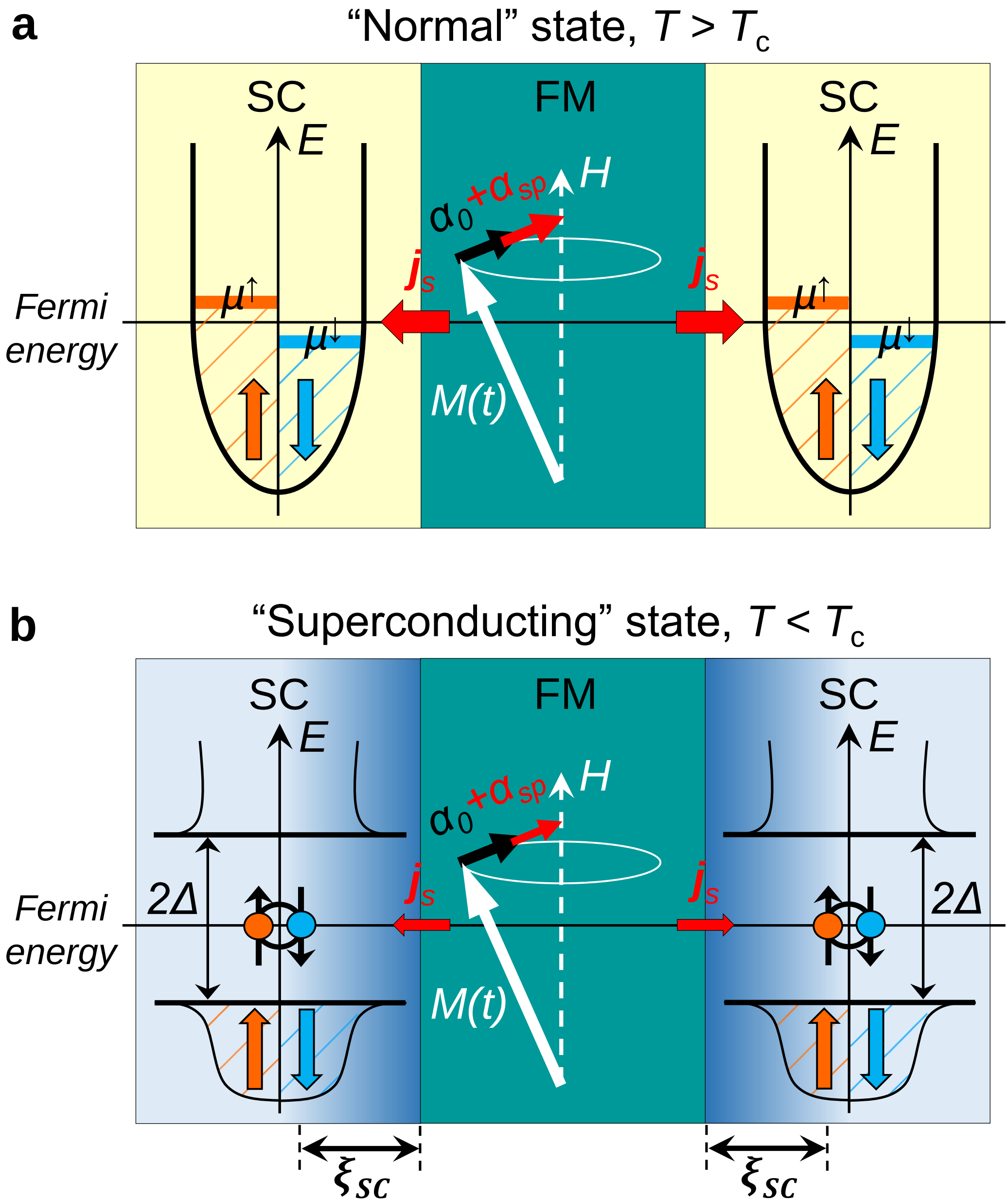

a
"Normal" state, T > Tc
SC
FM
SC
E
H
α0+αsp
js
μ↑
μ↓
Fermi energy
M(t)
b
"Superconducting" state, T < Tc
SC
FM
SC
E
H
α0+αsp
js
2Δ
Fermi energy
M(t)
ξsc

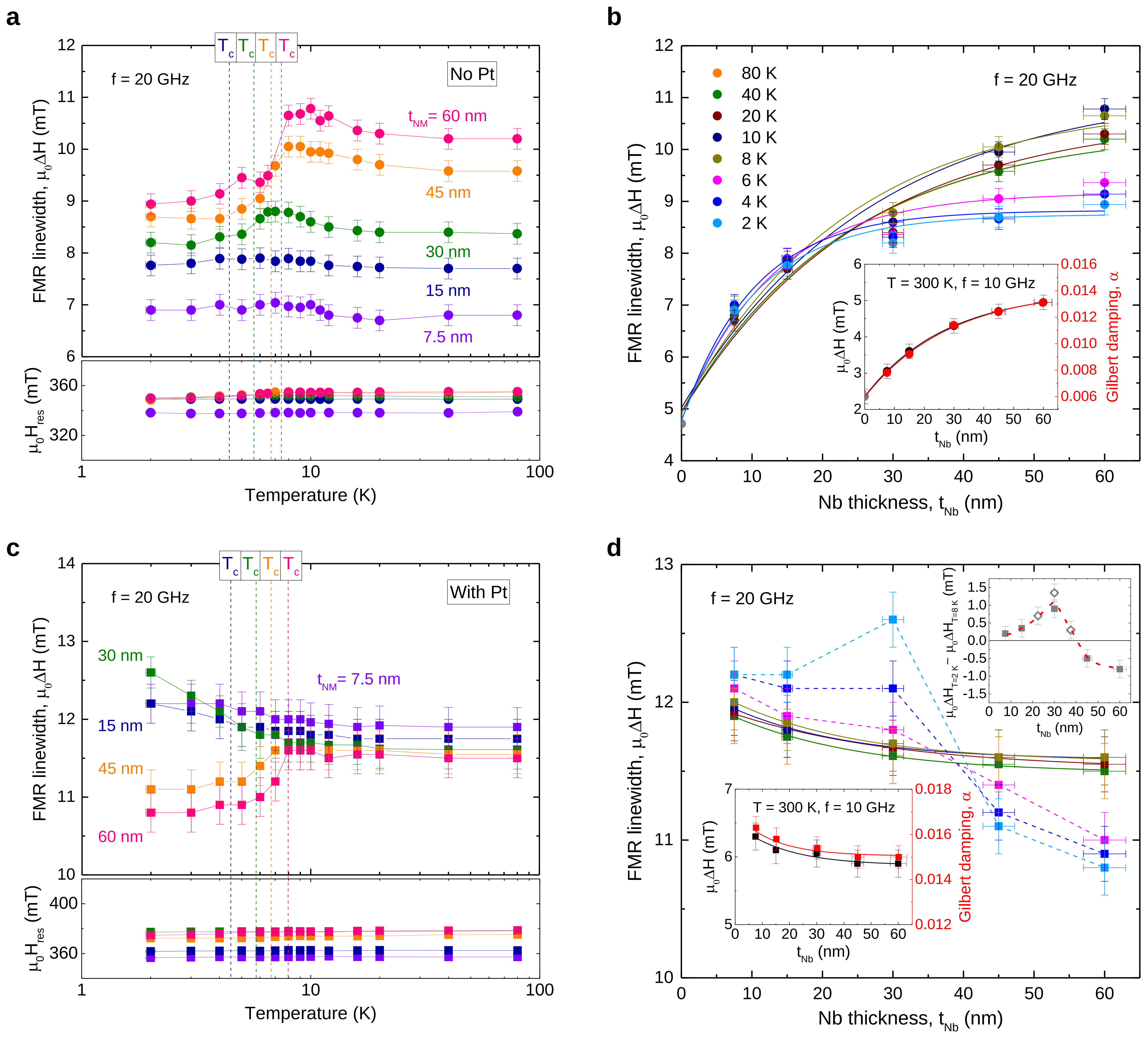

a
f = 20 GHz
No Pt
T_c T_c T_c T_c
t_{NM} = 60 nm
45 nm
30 nm
15 nm
7.5 nm
FMR linewidth, $\mu_0\Delta H$ (mT)
$\mu_0 H_{res}$ (mT)
Temperature (K)
b
80 K
40 K
20 K
10 K
8 K
6 K
4 K
2 K
f = 20 GHz
T = 300 K, f = 10 GHz
$\mu_0\Delta H$ (mT)
Gilbert damping, α
t_{Nb} (nm)
FMR linewidth, $\mu_0\Delta H$ (mT)
Nb thickness, t_{Nb} (nm)
c
f = 20 GHz
With Pt
T_c T_c T_c T_c
30 nm
15 nm
45 nm
60 nm
t_{NM} = 7.5 nm
FMR linewidth, $\mu_0\Delta H$ (mT)
$\mu_0 H_{res}$ (mT)
Temperature (K)
d
f = 20 GHz
$\mu_0\Delta H_{T=2\,K} - \mu_0\Delta H_{T=8\,K}$ (mT)
t_{Nb} (nm)
T = 300 K, f = 10 GHz
$\mu_0\Delta H$ (mT)
Gilbert damping, α
FMR linewidth, $\mu_0\Delta H$ (mT)
Nb thickness, t_{Nb} (nm)

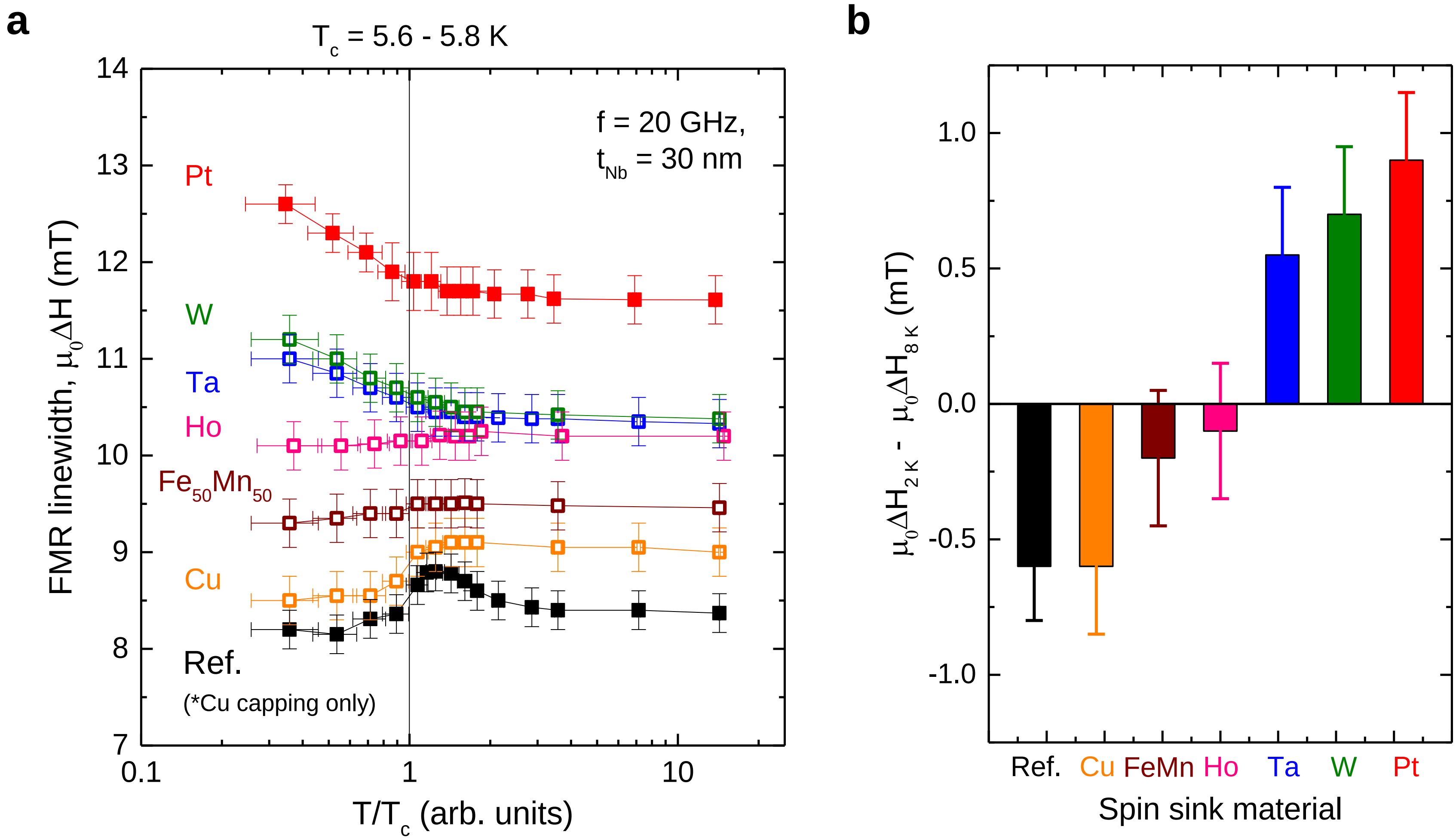
a
T_c = 5.6 - 5.8 K
f = 20 GHz,
t_{Nb} = 30 nm
Pt
W
Ta
Ho
$Fe_{50}Mn_{50}$
Cu
Ref.
(*Cu capping only)
FMR linewidth, $\mu_0\Delta H$ (mT)
T/T_c (arb. units)
b
$\mu_0\Delta H_{2\,K}$ - $\mu_0\Delta H_{8\,K}$ (mT)
Ref.
Cu
FeMn
Ho
Ta
W
Pt
Spin sink material